Journal of Experimental Medicine

BRIEF DEFINITIVE REPORT

Glymphatic system clears extracellular tau and protects from tau aggregation and neurodegeneration

Kazuhisa Ishida[1]*, Kaoru Yamada[1]*, Risa Nishiyama[1], Tadafumi Hashimoto[1,2,5], Itaru Nishida[1], Yoichiro Abe[3,4], Masato Yasui[3,4], and Takeshi Iwatsubo[1,5]

Accumulation of tau has been implicated in various neurodegenerative diseases termed tauopathies. Tau is a microtubule-associated protein but is also actively released into the extracellular fluids including brain interstitial fluid and cerebrospinal fluid (CSF). However, it remains elusive whether clearance of extracellular tau impacts tau-associated neurodegeneration. Here, we show that aquaporin-4 (AQP4), a major driver of the glymphatic clearance system, facilitates the elimination of extracellular tau from the brain to CSF and subsequently to deep cervical lymph nodes. Strikingly, deletion of AQP4 not only elevated tau in CSF but also markedly exacerbated phosphorylated tau deposition and the associated neurodegeneration in the brains of transgenic mice expressing P301S mutant tau. The current study identified the clearance pathway of extracellular tau in the central nervous system, suggesting that glymphatic clearance of extracellular tau is a novel regulatory mechanism whose impairment contributes to tau aggregation and neurodegeneration.

Introduction

The accumulation of tau protein inside of neurons has been implicated in a range of neurodegenerative disorders, including Alzheimer's disease (AD). As tau is a microtubule-associated protein, it was long believed that its localization was restricted to the cytoplasm of neurons. However, this classical view was recently challenged by several studies detecting tau in various extracellular fluids, e.g., brain interstitial fluid (ISF), cerebrospinal fluid (CSF), and blood plasma (Yamada et al., 2011; Sato et al., 2018; Barthélemy et al., 2020a). Tau release occurs independent of neuronal death via yet-to-be-identified unconventional secretory pathways and is regulated by neuronal activation (Pooler et al., 2013; Yamada et al., 2014; Wu et al., 2016). It has been shown that the production rate of CSF tau is significantly elevated in AD (Sato et al., 2018) and begins to increase prior to the symptomatic onset. In addition to such soluble tau species released into the extracellular space, it has been demonstrated that aggregated tau can also exit neurons (Kfoury et al., 2012). Once aggregated forms of tau are released, they are taken up by neurons and spread tau pathology in the brain (Clavaguera et al., 2009; Frost et al., 2009; Iba et al., 2013). Those studies reinforce the pathological significance of extracellular tau, which is further supported by the success of passive immunotherapy in reducing tau pathology and attenuating neurodegeneration in a mouse model of tauopathies (Yanamandra et al., 2013). Although these findings collectively led to the idea that targeting extracellular tau is therapeutic, how intrinsic clearance mechanisms might influence intracellular tau pathology has remained unexplored.

The presence of tau in the blood stream indicates that tau is cleared from the central nervous system to the periphery through extracellular fluids (Wang et al., 2018; Barthélemy et al., 2020a; Yanamandra et al., 2017). In general, substances released from brain cells are ultimately cleared from ISF by a combination of multiple pathways. These include local transport via the blood–brain barrier, phagocytosis by glial cells, receptor-mediated endocytosis by cerebral cells (Rauch et al., 2020; Cooper et al., 2021), and drainage into CSF. ISF drains into CSF via perivascular spaces of cerebral blood vessels by a mechanism termed the glymphatic pathway (Iliff et al., 2012). Cerebral arterial pulsation is a driving force of the glymphatic convective flow (Iliff et al., 2013), which is facilitated by water transport via aquaporin-4 (AQP4) expressed in perivascular astrocyte

---

[1]Department of Neuropathology, Graduate School of Medicine, The University of Tokyo, Tokyo, Japan; [2]Department of Innovative Dementia Prevention, Graduate School of Medicine, The University of Tokyo, Tokyo, Japan; [3]Department of Pharmacology, Keio University School of Medicine, Tokyo, Japan; [4]Keio University Global Research Institute, Center for Water Biology and Medicine, Tokyo, Japan; [5]National Institute of Neuroscience, National Center of Neurology and Psychiatry, Kodaira, Tokyo, Japan.

*K. Ishida and K. Yamada contributed equally to this paper. Correspondence to Kaoru Yamada: yamadaka@m.u-tokyo.ac.jp; Takeshi Iwatsubo: iwatsubo@m.u-tokyo.ac.jp.

https://doi.org/10.1084/jem.20211275

end-foot processes (Iliff et al., 2012; Mestre et al., 2018). Substances transported from brain parenchyma to CSF by the glymphatic system are then cleared out of the brain via dural lymphatic vessels (Aspelund et al., 2015). Glymphatic and lymphatic clearance was first discovered in rodent brains (Iliff et al., 2012; Louveau et al., 2015); however, magnetic resonance imaging studies revealed its presence in the human central nervous system (Eide et al., 2018; Ringstad et al., 2018). Glymphatic clearance was impaired in aged brain (Kress et al., 2014) and also associated with many neurodegenerative disorders (Ringstad et al., 2017). AQP4 single-nucleotide polymorphisms as well as reduced perivascular AQP4 localization have been reported in AD patients (Burfeind et al., 2017; Zeppenfeld et al., 2017). AQP4 deficiency has been shown to elicit ~70% reduction of Aβ clearance and also influence amyloid deposition and the associated neuronal functions in mice (Iliff et al., 2012; Xu et al., 2015; Abe et al., 2020). Although the glymphatic pathway plays a critical role in extracellular solute clearance, it is unknown how this pathway influences the accumulation of intracellular proteins in relation to its extracellular dynamics. The glymphatic system prevails during sleep and promotes waste clearance (Xie et al., 2013). Notably, extracellular tau levels are regulated by sleep–wake cycles in both mice and humans (Holth et al., 2019). Moreover, it has been shown that intracortically injected tau accumulated along a specific subset of large-caliber draining veins (Iliff et al., 2014). These observations inspired us to examine the involvement of the glymphatic pathway in tau clearance and a potential causal link between glymphatic clearance and tau-associated neurodegeneration.

Results and discussion

Tau is cleared from the brain to CSF by an AQP4-dependent mechanism

To gain insights into the mechanisms/kinetics of tau clearance in the brain, we performed microinjection of fluorescence-labeled tau and investigated whether tau is cleared via the glymphatic pathway by measuring the efflux clearance of tau into CSF of WT mice and AQP4 KO mice (Fig. 1 A). Quantification of the fluorescence-positive area on each brain slice revealed a biphasic change in HiLyte 555-human tau injected in the brain of WT mice. The fluorescence-positive area was first increased as tau spread within the brain and then decreased along with the clearance of tau over a period of ~12–48 h (Fig. 1, B and C). Notably, both processes of diffusion and clearance of tau were considerably suppressed in AQP4 KO mice, which led to significantly higher levels of tau retention at 48 h after injection compared to WT mice (Fig. 1 D). Analysis of tau drained into CSF by human-specific tau ELISA also revealed that AQP4 deficiency altered the dynamics of tau in CSF. In WT mice, HiLyte 555-human tau was drained into CSF by 6 h after injection and rapidly cleared (Fig. 1 E). In contrast, appearance of tau in CSF was significantly delayed in AQP4 KO mice and the CSF tau levels continued to increase (Fig. 1 E).

Tau drainage from CSF to deep cervical lymph nodes is impaired in AQP4 KO mice

CSF is absorbed by dural lymphatic vessels from the subarachnoid space and transported downstream into the deep cervical LNs (dcLNs; Da Mesquita et al., 2018; Aspelund et al., 2015). Continuous accumulation of tau in the CSF of AQP4 KO mice prompted us to hypothesize that this clearance pathway from CSF was compromised in AQP4 KO mice. To test this idea, we injected HiLyte 555-tau into CSF via the cisterna magna and examined the drainage into dcLNs (Fig. 2 A). One hour after injection, we observed an accumulation of tau in LYVE-1–positive dcLNs of WT mice, whereas the majority of AQP4 KO mice lacked accumulation of tau in dcLNs (Fig. 2, B and C). Consistent with this observation, AQP4 KO mice exhibited significantly higher levels of CSF tau (Fig. 2 D). These data suggested that CSF tau increase in AQP4 KO mice is likely attributed to impairment in tau drainage from CSF to dcLNs.

In addition to being cleared to dcLNs, a portion of substances in CSF move back into the brain along paravascular routes surrounding penetrating cerebral arteries. Previous studies have shown that this paravascular CSF influx also depends on AQP4 (Iliff et al., 2012; Mestre et al., 2018). Therefore, we investigated whether AQP4 deficiency influenced tau inflow from CSF to ISF. We observed that CSF tau moved into brain parenchyma through perivascular spaces of the cerebral arteries on pial surfaces more from the ventral surfaces of the brain compared to dorsal surfaces (Fig. 2 E). We observed that CSF tau entry into brain parenchyma was also impaired in AQP4 KO mice (Fig. 2, F–H) as with ovalbumin and dextran (Fig. S1), consistent with previous observations. The data highlight the significant roles of AQP4 in tau clearance into CSF, tau elimination from CSF via dcLNs, and CSF tau inflow into brains.

AQP4 deficiency exacerbated tau aggregation

Based on these observations that AQP4 impacts extracellular tau dynamics in brain parenchyma and CSF, we next asked how long-term deficiency of AQP4 impacts the tau aggregation and associated neurodegeneration. To this end, we crossed PS19 mice with AQP4 KO mice and pathologically examined the offspring at various ages. PS19 mice overexpress the FTDP-17–linked P301S mutant form of human tau and develop tau pathology and the associated neurodegeneration in an age-dependent manner (Yoshiyama et al., 2007). Although PS19 × AQP4 (+/+) at 6 months of age did not display phosphorylated tau pathology yet, tau accumulation was observed in the hippocampal CA3 region of PS19 × AQP4 (−/−) (Fig. 3 A). Although PS19 × AQP4 (−/−) mice at this age did not display overt neuronal loss that is evident in aged PS19 mice, they exhibited significant elevation of CSF tau (Fig. 3, A and B), suggesting that altered tau dynamics in CSF precedes tau aggregation and neurodegeneration. At 9 months of age, massive deposition of phosphorylated tau in PS19 × AQP4 (−/−) became more evident compared to PS19 × AQP4 (+/+). Extensive deposition of phosphorylated tau positive both for AT8 and PHF-1 antibodies was seen in the neuronal cell bodies and neuropil neurites of the medial temporal area and cerebral neocortices of PS19 × AQP4 (−/−) (Fig. 3 C and Fig. S2 A). Quantification of AT8 immunolabeled areas revealed that AQP4 deficiency markedly exacerbates tau deposition in multiple brain regions including the hippocampus, amygdala, thalamus, and cerebral neocortices (Fig. 3 D). Staining with the MC1 antibody that recognizes tau with a disease-associated conformation was stronger in the brains of PS19 × AQP4 (−/−) mice

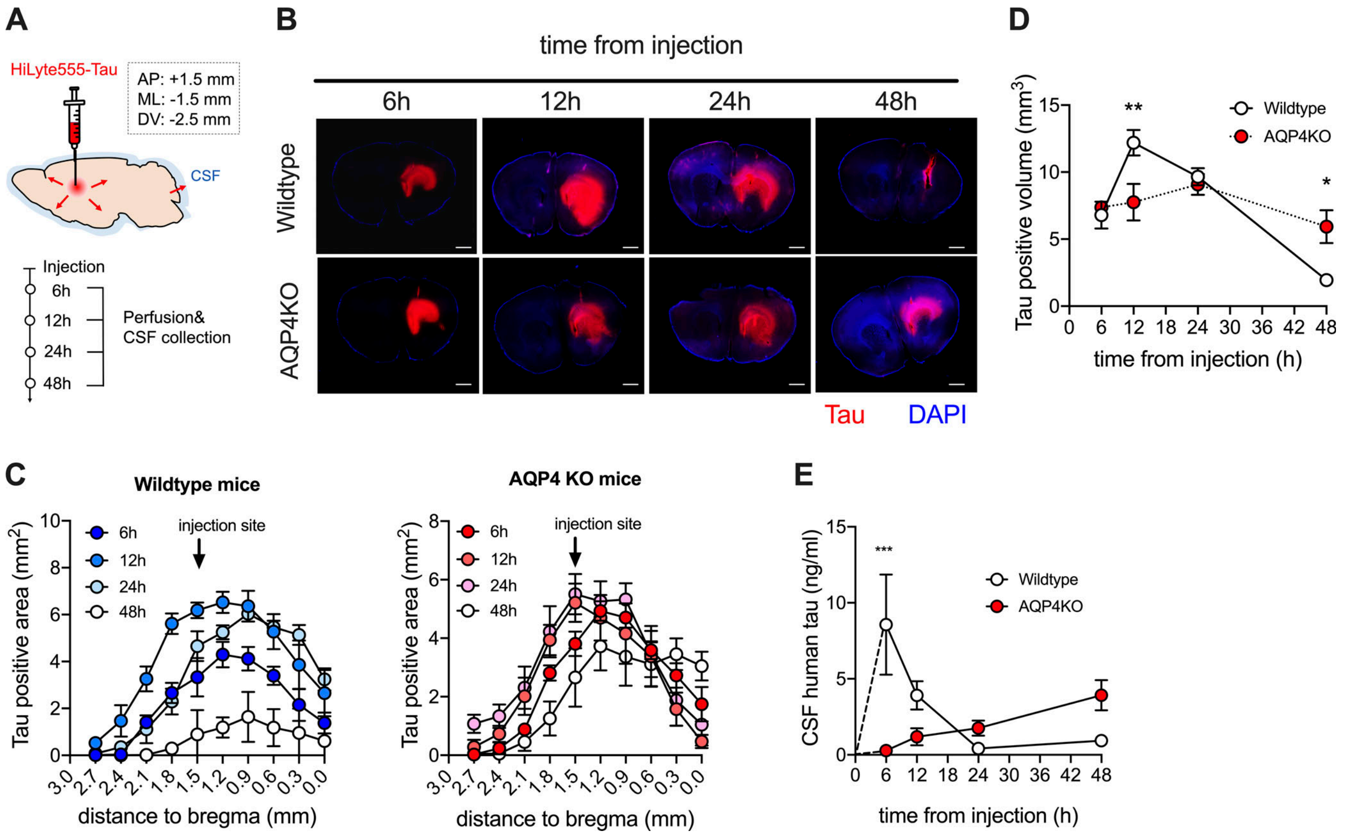

Figure 1. **Tau is cleared from the brain to CSF in an AQP4-dependent manner. (A)** HiLyte 555–labeled human tau was stereotaxically injected into the brain. At 6, 12, 24, and 48 h after injection, the remaining tau in the brain and CSF tau levels were assessed. **(B)** Representative brain sections around the injection site with DAPI counterstaining. Scale bars, 1 mm. **(C)** Tau-positive area (mm^2) was plotted with arrows that indicate injection sites. WT mice (*n* = 5), AQP4 KO mice (*n* = 6 for 12 h and 24 h, *n* = 5 for 6 h and 48 h). **(D)** Tau-positive volume (mm^3) at different time points from injection. Two-way ANOVA with Bonferroni post-hoc analysis; *, P < 0.05; **, P < 0.01. *n* = 5/group. **(E)** CSF human tau levels at 6 (*n* = 5), 12 (*n* = 5), 24 (*n* = 5), and 48 h (*n* = 6) with hypothetical human tau concentration at 0 h were plotted. Two-way ANOVA with Bonferroni post-hoc analysis; ***, P < 0.001.

(Fig. S2, B and C). We further biochemically examined the aggregation status of tau deposited in the brain and found a significant increase in the levels of insoluble human tau in formic acid fractions of 9-month-old PS19 × AQP4 (−/−) mice (Fig. 3, E and F).

LRP1 is an endocytotic receptor for extracellular tau and impacts tau aggregation by promoting its spreading (Rauch et al., 2020). LRP1 was primarily detected in cortical neuronal membranes, whereas its expression in vasculatures was not clearly stained compared to AQP4 (Fig. S3 A). LRP1 expression levels as well as tissue distribution were comparable between PS19 × AQP4 (+/+) and PS19 × AQP4 (−/−), suggesting that enhanced tau deposition was not likely due to changes in the expression of LRP1 (Fig. S3, B and C).

AQP4 deficiency exacerbated tau-associated neurodegeneration

9-month-old PS19 × AQP4 (−/−) mice exhibited severe brain atrophy with noticeably thinner cortices and hippocampus compared to PS19 × AQP4 (+/+) (Fig. 4 A). Ventricular dilatation, which is often associated with brain atrophy in PS19, was more prominent in PS19 × AQP4 (−/−) (Fig. 4, A and B). To examine whether such brain atrophy involves neuronal loss, brain sections were stained with NeuN antibody. The numbers of dentate granule cells and pyramidal cell layer neurons in the piriform cortex positive for NeuN also were significantly decreased in PS19 × AQP4 (−/−) compared to PS19 × AQP4 (+/+) (Fig. 4, C and D). Notably, these neurodegenerative phenotypes were not observed in younger (3- and 6-month-old) PS19 × AQP4 (−/−) mice or AQP4 KO mice that were not crossed with PS19 (Fig. 4, E and F), suggesting that AQP4 only modulated tau-driven neurodegeneration. PS19 × AQP4 (+/−) exhibited an intermediate level of neuropathology between PS19 × AQP4 (+/+) and PS19 × AQP4 (−/−), suggesting a dosage-dependent effect of AQP4 (Fig. S2 A).

The glymphatic system denotes a brain-wide pathway to eliminate substances in the extracellular fluid (Iliff et al., 2012). However, how it impacts the neurodegeneration associated with deposition of pathogenic proteins that normally reside inside of neurons (e.g., tau), in relation to its extracellular dynamics, remained elusive. We have shown that extracellular tau is cleared from the brain to CSF by an AQP4-dependent mechanism. AQP4 deficiency not only impacted tau clearance from brain parenchyma but also from CSF to dcLNs, which has been shown to be mediated by the lymphatic system (Aspelund et al., 2015). The defect of CSF tau drainage into dcLN could be due to the potential involvement of AQP4 on the lymphatic clearance. Alternatively, it is also possible that a crosstalk between glymphatic and

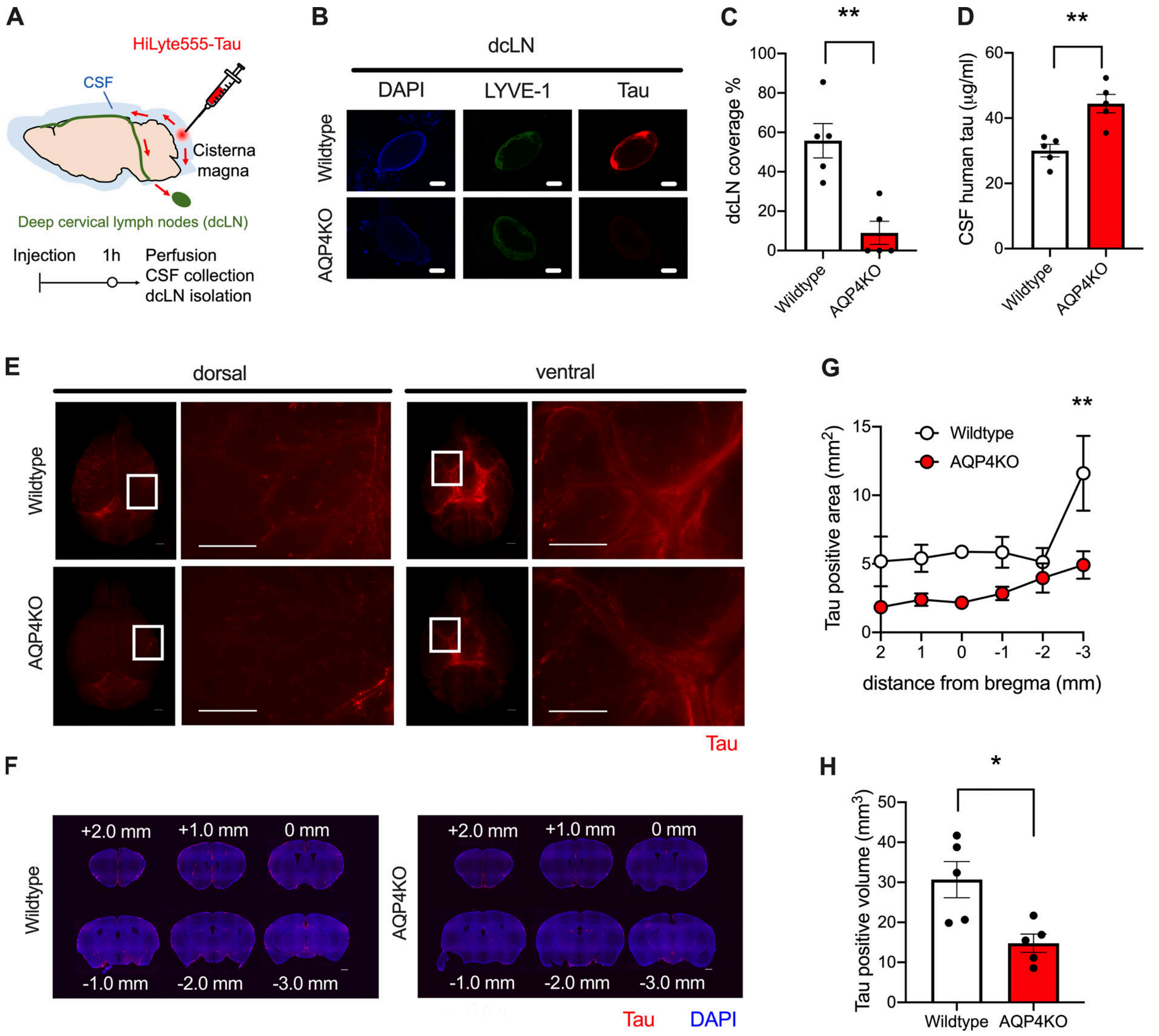

Figure 2. **Tau clearance from CSF to dcLNs and influx into the brain occur in an AQP4-dependent manner. (A)** At 1 h from intracisternal injection of HiLyte 555–labeled tau, CSF, brains, and dcLNs were analyzed. **(B)** Representative images of tau accumulation (red) in LYVE-1–positive dcLNs (pseudocolored green) with DAPI counterstaining (blue). Scale bars, 1 mm. **(C)** Percent area covered by tau in dcLNs. Unpaired two-tailed test; **, $P < 0.01$. $n = 5$/group. **(D)** CSF tau levels. Unpaired two-tailed test; **, $P < 0.01$. $n = 5$/group. **(E)** Representative images of tau accumulation (red). Scale bars, 1 mm. **(F)** Representative brain sections showing tau (red) accumulation with DAPI staining (blue). Scale bars, 1 mm. **(G)** Tau-positive area (mm^2). Two-way ANOVA with Bonferroni post-hoc analysis; **, $P < 0.01$. $n = 5$/group. **(H)** Average tau-positive volume (mm^3). Unpaired two-tailed test; *, $P < 0.05$. $n = 5$/group.

lymphatic clearance might contribute to impaired tau clearance from CSF to dcLNs in AQP4 KO mice. Consistent with this idea, it has been shown that ablating lymphatic vessels with genetic manipulation or surgical ligation elevated tau levels in the brain (Patel et al., 2019; Cao et al., 2018).

Although a previous study has also suggested the involvement of AQP4 in ISF outflow of exogenous tau (Harrison et al., 2020), it remained elusive how the glymphatic system impacts the dynamics of extracellular tau produced in the mouse brain as well as tau-associated neurodegeneration. We showed that AQP4 KO mice exhibited a significant elevation of CSF tau, which occurred prior to overt neurodegeneration in PS19 mice. It has been suggested that an increase in CSF tau in AD reflects the degree of neurodegeneration, i.e., a passive release of tau from neurons to extracellular fluids. Our finding that an impairment in clearance led to the significant elevation of CSF tau suggests that tau levels in CSF are more dynamically regulated than previously conceptualized (Barthélemy et al., 2020b).

The most striking finding in this study is that altered clearance of extracellular tau by AQP4 deficiency was associated with tau deposition and neurodegeneration. A recent study showed that the perivascular expression of AQP4 was reduced in the rTg4510 mouse model of tauopathies, which resulted in a decrease in ISF–CSF exchange of tau (Harrison et al., 2020). Taken together with our current findings that AQP4 deficiency exacerbated tau aggregation, a vicious cycle might exist between glymphatic clearance and tau aggregation.

The detailed mechanisms of how the impairment in clearing extracellular tau led to the exacerbation of tau-related pathology require further investigations. One possible explanation for the

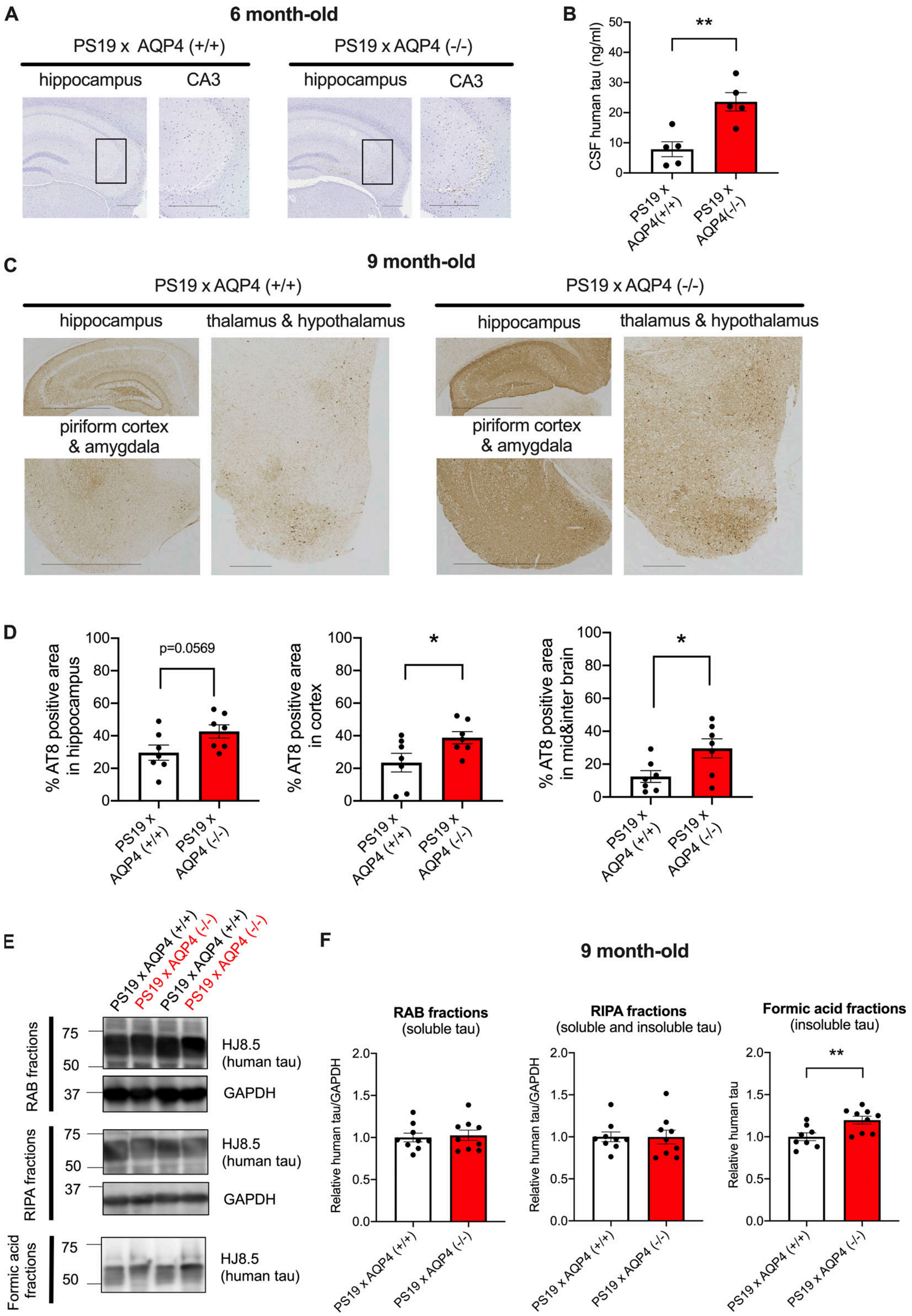

Figure 3. **AQP4 deficiency markedly exacerbates tau pathology in PS19 mice. (A)** Representative images of AT8 staining in 6-month-old mice with hematoxylin staining. Scale bars, 300 µm. **(B)** CSF human tau levels in 6-month-old mice. Unpaired two-tailed *t* test; **, P < 0.01. *n* = 5/group. **(C)** Representative images of AT8 staining in 9-month-old mice. Scale bars, 1 mm for the hippocampus, piriform cortex, and amygdala and 300 µm for the thalamus and hypothalamus. **(D)** Quantification of the percentage of area covered by AT8 staining in 9-month-old mice. Unpaired two-tailed *t* test; *, P < 0.05. *n* = 7/group. **(E)** Representative immunoblots probing for human tau and GAPDH in RAB, RIPA, and formic acid fractions of 9-month-old PS19 × AQP4 (+/+) and PS19 × AQP4 (−/−) mice (in kD). **(F)** Quantification of immunoblot probing for human tau in RAB, RIPA, and formic acid fractions of 9-month-old PS19 × AQP4 (+/+) (*n* = 8 or 9) and PS19 × AQP4 (−/−) mice (*n* = 9). Unpaired two-tailed *t* test; **, P < 0.01. Source data are available for this figure: SourceData F3.

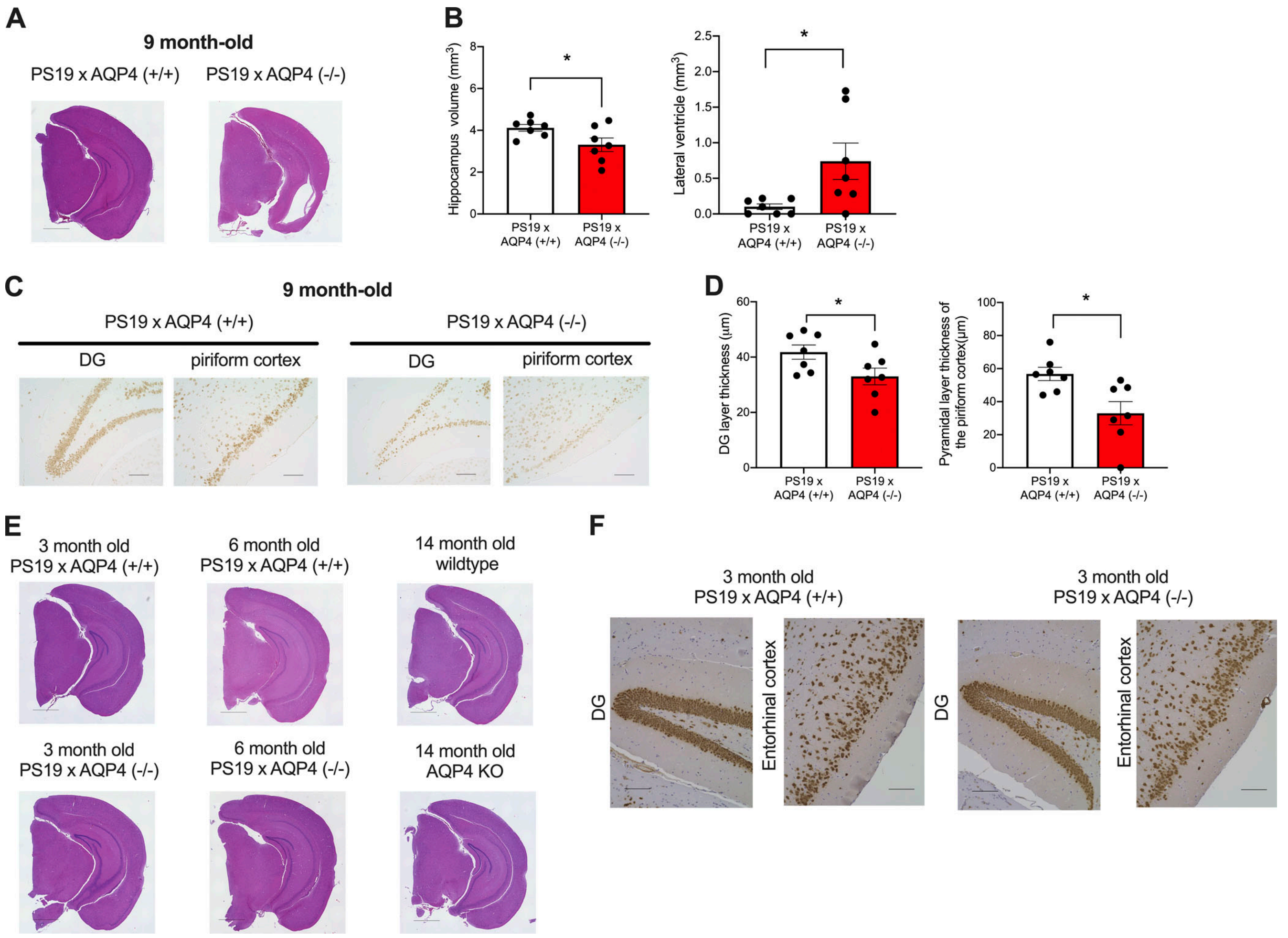

Figure 4. **AQP4 deficiency markedly exacerbates neurodegeneration in PS19 mice. (A)** Representative images of 9-month-old mice stained with H&E staining. Scale bars, 1 mm. **(B)** Quantification of volume of hippocampus and lateral ventricle in 9-month-old mice. Unpaired two-tailed test; *, $P < 0.05$. $n = 7$/group. **(C)** Representative images of NeuN staining in DG and piriform cortex of 9-month-old mice. Scale bars, 100 μm. **(D)** Quantification of the thickness of granule cell layer in DG and the pyramidal cell layer in the piriform cortex of 9-month-old mice. Unpaired two-tailed test; *, $P < 0.05$. $n = 7$/group. **(E)** Representative images of 3- and 6-month-old PS19 × AQP4 (+/+) mice and 14-month-old WT mice or AQP4 KO mice stained with H&E. Scale bars, 1 mm. **(F)** Representative images of NeuN staining in 3-month-old PS19 × AQP4 (+/+) and PS19 × AQP4 (−/−) mice counter-stained with hematoxylin. Scale bars, 100 μm.

exacerbated tau pathology in AQP4-deficient PS19 mice would be that the impairment of tau clearance promotes the spreading of pathological tau species to other cells. Alternatively, the intracellular tau might be in a unique equilibrium with extracellular tau under certain conditions (Yamada et al., 2011), where tau levels in both compartments could be ultimately modulated by the glymphatic clearance. Investigating the underlying mechanisms will lead to better understanding of how dynamics of different forms of tau is coupled between the extracellular and intracellular compartments. In summary, our current findings highlight the previously unrecognized, unique interplay between extracellular tau clearance and tau pathophysiology and also motivate future therapies targeting modulation of extracellular tau.

Materials and methods

Study design

All animal experiments were reviewed and approved by the Institutional Animal Care and Use Committee of the Graduate School of Medicine at the University of Tokyo. Mice associated with unsuccessful CSF collection or injection failure or insufficient transcardial perfusion or significant intracerebral bleeding were excluded for analysis.

Mice

WT male and female mice on a C57B6/J background were purchased from Japan SLC (Hamamatsu). *Aqp4*$^{-/-}$ mice were generated and maintained as previously described (Ikeshima-Kataoka et al., 2013; RIKEN BioResource Research Center accession no. CDB0758K: http://www.cdb.riken.jp/arg/mutant%20mice%20list.html). PS19 mice overexpressing P301S mutant tau (stock number: 008169 Jackson laboratory; Yoshiyama et al., 2007) were crossed with *Aqp4*$^{-/-}$ mice, and F2 generation was used for analysis. Both male and female mice were used for the experiments.

Recombinant tau purification and labeling

Recombinant tau (2N4R isoform) was purified as previously described (Tanaka et al., 2019; Aoyagi et al., 2007). Tau was incubated with NH_2-reactive HiLyte Fluor 555 (Dojindo) according to the manufacturer's instructions.

Stereotaxic injection of HiLyte 555 tau in brains

Mice ranging from 3 to 4 months of age were anesthetized by intraperitoneal injection of a combination anesthetic of 0.75 mg/kg medetomidine, 4.0 mg/kg midazolam, and 5.0 mg/kg butorphanol and secured in a stereotaxic frame. Mice were then injected with 1 µl of HiLyte 555-tau (100 µg/ml) in the striatum (bregma: +1.5 mm, lateral: −1.5 mm, depth: −2.5 mm) using a 1701RN NEUROS SYRINGE (Hamilton) at a rate of 0.1 µl/min. At 6, 12, 24, and 48 h after injection, CSF was collected from the cisterna magna and mice were transcardially perfused with 4% paraformaldehyde in PBS. Brains were dissected and immersed in 4% PFA and postfixed overnight. Fixed brains were sliced at 100 µm thickness with a LinearSlicer PRO7 (Dosaka EM) and mounted with PROLONG Anti-Fade Gold with DAPI (Thermo Fisher Scientific).

Intra-cisterna magna injection

Five-month-old WT mice were anesthetized, and the skin of the neck was shaved and an incision was made. The muscle layers were bluntly dissected and the dura mater overlaying the cisterna magna was exposed. For injection, 10 µl of HiLyte 555-tau (200 µg/ml) or Alexa488-ovalbumin (Thermo Fisher Scientific, 5 mg/ml) or Dextran, Texas Red, 3,000 MW, Neutral (Thermo Fisher Scientific, 5 mg/ml) was injected into the subarachnoid space at a rate of 1 µl/min using a syringe pump. To minimize possible influences of the sleep/wake status on glymphatic flows, injection was initiated at a similar time of day. After injecting, the syringe was left in place for an additional 25 min to prevent backflow of CSF and 50% of the initial dose of anesthesia was administered. 1 h after tracer injection, CSF was collected and the mice were transcardially perfused with 4% paraformaldehyde in PBS. Brains and dcLNs were dissected and immersed in 4% PFA and postfixed overnight. Fixed brains were sliced at 100 µm thickness with a LinearSlicer PRO7 (Dosaka EM) and mounted with PROLONG Anti-Fade Gold with DAPI (Thermo Fisher Scientific).

Histochemistry/immunohistochemistry

To examine the tau pathology in brains, fixed hemi-brains were embedded in paraffin blocks and sectioned coronally at 4 µm thickness for histochemical analysis. De-paraffinized brain sections were stained with H&E or immunostained using AT8 antibody (MN1020B; Thermo Fisher Scientific), PHF-1 antibody, MC1 antibody (kind gifts from Dr. Peter Davies, Albert Einstein College of Medicine, Bronx, NY), LRP1 antibody (ab92554; Abcam), NeuN antibody (MAB377; Sigma-Aldrich), or AQP4 antibody (A5971; Sigma-Aldrich). For antigen retrieval, de-paraffinzed sections were treated with microwave (550 W, 10 min) in citrate buffer (pH 6.0) prior to immunostaining. To detect proteinase K resistant tau inclusion, sections were treated with 100 µg/ml proteinase K for 6 min at 37°C prior to AT8 and PHF-1 staining (Iba et al., 2013).

To detect tau accumulation, isolated dcLNs were embedded in 4% NuSieve GTG agarose after carefully removing fatty tissue and sliced at 100 µm thickness with a LinearSlicer PRO7 (Dosaka EM). The sections were blocked with 10% calf serum for 30 min and incubated with anti–LYVE-1 antibody (ab14917; Abcam) and washed and incubated with goat anti-Rabbit IgG (H + L) Highly Cross-Adsorbed Secondary Antibody, Alexa Fluor 647 (A-21245; Thermo Fisher Scientific). The sections were then mounted with PROLONG Anti-Fade Gold with DAPI (Thermo Fisher Scientific).

Biochemistry

Cortices were homogenized with reassembly buffer (RAB) containing cOmplete protease inhibitor cocktails (Roche) and PhosSTOP (Roche) and ultracentrifuged at 4°C (Yamada et al., 2011). Supernatants were saved as RAB soluble fractions and stored at −80°C. RAB insoluble pellets were homogenized with radioimmunoprecipitation assay (RIPA) buffer containing cOmplete protease inhibitor cocktails (Roche) and PhosSTOP (Roche) and ultracentrifuged at 4°C. Supernatants were saved as RIPA soluble fractions and stored at −80°C. RIPA insoluble pellets were homogenized with 70% formic acid and ultracentrifuged at 4°C. Supernatants were saved as formic acid soluble fractions and stored at −80°C. Formic acid soluble fractions were dialyzed against PBS supplemented with 0.5 mM phenylmethylsulfonyl fluoride prior to immunoblotting.

Immunoblots

Fractionated brain homogenates were dissolved in lithium dodecyl sulfate sample buffer (Novex) containing 2% β-mercaptothanol. Proteins were separated in Tris-Glycine gel and transferred to poly vinylidene difluoride membranes and incubated with an anti-LRP1 antibody 11H4 (a kind gift from Dr. Ayae Kinoshita, Kyoto University, Kyoto, Japan), an anti-actin antibody (A2066-100uL; Sigma-Aldrich), an anti-human tau HJ8.5 antibody (a kind gift from Dr. David Holtzman, Washington University, St. Louis, MO), or an anti-GAPDH antibody (016-25523; FUJIFILM Wako Pure Chemical Corporation), followed by species-specific HRP-conjugated secondary antibodies. Bands were visualized using ImmunoStar (FUJIFILM Wako Pure Chemical Corporation), and signals were detected using ImageQuant LAS-4000 (GE healthcare). Bands were quantified using ImageQuant TL (GE healthcare).

Image analysis

Brain sections were imaged using BZ-X710 (Keyence). For volumetric analysis, three coronal sections per mouse stained with AT8 (bregma −2.0 mm, −2.5 mm, −3.5 mm) were imaged, and the total volume was calculated based on the volume between two sections, which was determined using the following formula: the volume between two sections = (average of areas) × (distance between the sections) mm. Quantification of fluorescence was performed in nonprocessed images. To assess signals from HiLyte 555-tau in the brain or dcLNs, HiLyte 555positive areas above the threshold were binalized, and the percentages covered by positive area were quantified using ImageJ (National Institutes of Health). For fluorescent images, adjustments of brightness and contrast have been equally applied to the entire image. Percentage of areas stained by AT8 in selected brain regions was also quantified using ImageJ (National Institutes of

Health). Neuronal cell layer thickness of dentate granule cell layers or pyramidal cell layers in the piriform cortex was measured using a scale perpendicular to the layer in two or three coronal sections stained with NeuN antibody. Quantification of hippocampus volume, lateral ventricle volume, AT8 staining in cortex, mid- and inter-brain regions, dentate gyrus (DG) layer thickness, and pyramidal layer thickness in the piriform cortex was performed by an investigator blinded to sample IDs. Quantification of the AT8-positive area was performed independently by multiple investigators to ensure reproducibility.

Human specific tau ELISA

Concentrations of human tau were quantified by sandwich ELISAs using Tau-5 as a coating antibody and biotinylated HT7 (MN1000B; Thermo Fisher Scientific) as a detection antibody as described previously (Yamada et al., 2015).

Statistics

Sample sizes for the experiments were determined based on prior publications using PS19 mice. All data were presented as mean ± SEM. Measurements were taken from distinct samples. Statistical analysis was performed using GraphPad Prism 8.4.3 (GraphPad Software). The normality of the data was verified using a Shapiro-Wilk test. Significance was determined by a two-tailed unpaired *t* test or two-way ANOVA with Bonferroni post-hoc analysis. Statistically significant outliers ($P > 0.05$) were identified by Grubb's test and omitted from further analysis.

Data availability

The data that support the findings of this study are available from the corresponding authors upon reasonable request.

Online supplemental material

Fig. S1 shows representative brain images of ovalbumin and dextran accumulation; quantification of the ovalbumin-positive area; and quantification of ovalbumin-positive volume. Fig. S2 shows representative images of PHF-1 staining; representative images of MC1 staining; and quantification of MC1-positive area. Fig. S3 shows representative images of LRP1 and AQP4 staining; immunoblot probing for LRP1 and actin; and quantification of immunoblot probing for LRP1.

Acknowledgments

We thank Yuko Matsuo for technical assistance for animal husbandry. We also thank Drs. Tsuneo Nakajima and Shuko Takeda for valuable advice for CSF collection. We also thank members in Iwatsubo's laboratory for helpful suggestions and discussion.

This study was supported partially by Japan Science and Technology Agency Core Research for Evolutional Science and Technology (Grant No. JPMJCR18H3; K. Yamada), the program for Brain Mapping by Integrated Neurotechnologies for Disease Studies from Japan Agency for Medical Research and development (Grant No. JP20dm0207073; K. Yamada and T. Hashimoto), Grant-in-Aid for Scientific Research (C; Grant No. 18K07388; K. Yamada), the Collaborative Research Project (2021-20012) of Brain Research Institute, Niigata University (K. Yamada), Grant-in-Aid for Scientific Research (A; Grant No. 20H00525; T. Iwatsubo) and a collaborative grant from NIPRO Co. (T. Iwatsubo and K. Yamada), and Grant-in-Aid for Scientific Research (B; Grant No. 18H02606; M. Yasui).

Author contributions: K. Yamada conceived the idea with critical input from K. Ishida, T. Hashimoto, I. Nishida, Y. Abe, M. Yasui, and T. Iwatsubo. K. Ishida and K. Yamada designed the study and performed the experiments. K. Ishida, K. Yamada, and R. Nishiyama analyzed the data. K. Yamada and T. Iwatsubo supervised the study. K. Yamada wrote the manuscript and T. Iwatsubo edited the manuscript. All authors read and approved the manuscript.

Disclosures: K. Yamada reported "part of the study was supported by a collaborative grant from NIPRO Co." No other disclosures were reported.

Submitted: 11 June 2021
Revised: 21 December 2021
Accepted: 24 January 2022

References

Abe, Y., N. Ikegawa, K. Yoshida, K. Muramatsu, S. Hattori, K. Kawai, M. Murakami, T. Tanaka, W. Goda, M. Goto, et al. 2020. Behavioral and electrophysiological evidence for a neuroprotective role of aquaporin-4 in the 5xFAD transgenic mice model. *Acta Neuropathol. Commun.* 8:67. https://doi.org/10.1186/s40478-020-00936-3

Aoyagi, H., M. Hasegawa, and A. Tamaoka. 2007. Fibrillogenic nuclei composed of P301L mutant tau induce elongation of P301L tau but not wild-type tau. *J. Biol. Chem.* 282:20309–20318. https://doi.org/10.1074/jbc.M611876200

Aspelund, A., S. Antila, S.T. Proulx, T.V. Karlsen, S. Karaman, M. Detmar, H. Wiig, and K. Alitalo. 2015. A dural lymphatic vascular system that drains brain interstitial fluid and macromolecules. *J. Exp. Med.* 212: 991–999. https://doi.org/10.1084/jem.20142290

Barthélemy, N.R., K. Horie, C. Sato, and R.J. Bateman. 2020a. Blood plasma phosphorylated-tau isoforms track CNS change in Alzheimer's disease. *J. Exp. Med.* 217:1–12:e20200861. https://doi.org/10.1084/JEM.20200861

Barthélemy, N.R., Y. Li, N. Joseph-Mathurin, B.A. Gordon, J. Hassenstab, T.L.S. Benzinger, V. Buckles, A.M. Fagan, R.J. Perrin, A.M. Goate, et al. 2020b. A soluble phosphorylated tau signature links tau, amyloid and the evolution of stages of dominantly inherited Alzheimer's disease. *Nat. Med.* 26:398–407. https://doi.org/10.1038/s41591-020-0781-z

Burfeind, K.G., C.F. Murchison, S.K. Westaway, M.J. Simon, D. Erten-Lyons, J.A. Kaye, J.F. Quinn, and J.J. Iliff. 2017. The effects of noncoding aquaporin-4 single-nucleotide polymorphisms on cognition and functional progression of Alzheimer's disease. *Alzheimers Dement.* 3:348–359. https://doi.org/10.1016/J.TRCI.2017.05.001

Cao, X., H. Xu, W. Feng, D. Su, and M. Xiao. 2018. Deletion of aquaporin-4 aggravates brain pathology after blocking of the meningeal lymphatic drainage. *Brain Res. Bull.* 143:83–96. https://doi.org/10.1016/j.brainresbull.2018.10.007

Clavaguera, F., T. Bolmont, R.A. Crowther, D. Abramowski, S. Frank, A. Probst, G. Fraser, A.K. Stalder, M. Beibel, M. Staufenbiel, et al. 2009. Transmission and spreading of tauopathy in transgenic mouse brain. *Nat. Cell Biol.* 11:909–913. https://doi.org/10.1038/ncb1901

Cooper, J.M., A. Lathuiliere, M. Migliorini, A.L. Arai, M.M. Wani, S. Dujardin, S.C. Muratoglu, B.T. Hyman, and D.K. Strickland. 2021. Regulation of tau internalization, degradation, and seeding by LRP1 reveals multiple pathways for tau catabolism. *J. Biol. Chem.* 296:100715. https://doi.org/10.1016/j.jbc.2021.100715

Eide, P.K., S.A.S. Vatnehol, K.E. Emblem, and G. Ringstad. 2018. Magnetic resonance imaging provides evidence of glymphatic drainage from human brain to cervical lymph nodes. *Sci. Rep.* 8:7194–7210. https://doi.org/10.1038/s41598-018-25666-4

Frost, B., R.L. Jacks, and M.I. Diamond. 2009. Propagation of tau misfolding from the outside to the inside of a cell. *J. Biol. Chem.* 284:12845–12852. https://doi.org/10.1074/jbc.M808759200

Harrison, I.F., O. Ismail, A. Machhada, N. Colgan, Y. Ohene, P. Nahavandi, Z. Ahmed, A. Fisher, S. Meftah, T.K. Murray, et al. 2020. Impaired glymphatic function and clearance of tau in an Alzheimer's disease model. *Brain.* 143:2576–2593. https://doi.org/10.1093/brain/awaa179

Holth, J.K., S.K. Fritschi, C. Wang, N.P. Pedersen, J.R. Cirrito, T.E. Mahan, M.B. Finn, M. Manis, J.C. Geerling, P.M. Fuller, et al. 2019. The sleep-wake cycle regulates brain interstitial fluid tau in mice and CSF tau in humans. *Science.* 363:880–884. https://doi.org/10.1126/science.aav2546

Iba, M., J.L. Guo, J.D. McBride, B. Zhang, J.Q. Trojanowski, and V.M.-Y. Lee. 2013. Synthetic tau fibrils mediate transmission of neurofibrillary tangles in a transgenic mouse model of Alzheimer's-like tauopathy. *J. Neurosci.* 33:1024–1037. https://doi.org/10.1523/JNEUROSCI.2642-12.2013

Ikeshima-Kataoka, H., Y. Abe, T. Abe, and M. Yasui. 2013. Immunological function of aquaporin-4 in stab-wounded mouse brain in concert with a pro-inflammatory cytokine inducer, osteopontin. *Mol. Cell. Neurosci.* 56:65–75. https://doi.org/10.1016/j.mcn.2013.02.002

Iliff, J.J., M.J. Chen, B.A. Plog, D.M. Zeppenfeld, M. Soltero, L. Yang, I. Singh, R. Deane, and M. Nedergaard. 2014. Impairment of glymphatic pathway function promotes tau pathology after traumatic brain injury. *J. Neurosci.* 34:16180–16193. https://doi.org/10.1523/JNEUROSCI.3020-14.2014

Iliff, J.J., M. Wang, Y. Liao, B.A. Plogg, W. Peng, G.A. Gundersen, H. Benveniste, G.E. Vates, R. Deane, S.A. Goldman, et al. 2012. A paravascular pathway facilitates CSF flow through the brain parenchyma and the clearance of interstitial solutes, including amyloid. *Sci. Transl. Med.* 4:147ra111. https://doi.org/10.1126/scitranslmed.3003748

Iliff, J.J., M. Wang, D.M. Zeppenfeld, A. Venkataraman, B.A. Plog, Y. Liao, R. Deane, and M. Nedergaard. 2013. Cerebral arterial pulsation drives paravascular CSF-interstitial fluid exchange in the murine brain. *J. Neurosci.* 33:18190–18199. https://doi.org/10.1523/JNEUROSCI.1592-13.2013

Kfoury, N., B.B. Holmes, H. Jiang, D.M. Holtzman, and M.I. Diamond. 2012. Trans-cellular propagation of tau aggregation by fibrillar species. *J. Biol. Chem.* 287:19440–19451. https://doi.org/10.1074/jbc.M112.346072

Kress, B.T., J.J. Iliff, M. Xia, M. Wang, H.S. Wei Bs, D. Zeppenfeld, L. Xie, H. Kang, Q. Xu, J.A. Liew, et al. 2014. Impairment of paravascular clearance pathways in the aging brain. *Ann. Neurol.* 76:845–861. https://doi.org/10.1002/ana.24271

Louveau, A., I. Smirnov, T.J. Keyes, J.D. Eccles, S.J. Rouhani, J.D. Peske, N.C. Derecki, D. Castle, J.W. Mandell, K.S. Lee, et al. 2015. Structural and functional features of central nervous system lymphatic vessels. *Nature.* 523:337–341. https://doi.org/10.1038/nature14432

Da Mesquita, S., A. Louveau, A. Vaccari, I. Smirnov, R.C. Cornelison, K.M. Kingsmore, C. Contarino, S. Onengut-Gumuscu, E. Farber, D. Raper, et al. 2018. Functional aspects of meningeal lymphatics in ageing and Alzheimer's disease. *Nature.* 560:185–191. https://doi.org/10.1038/s41586-018-0368-8

Mestre, H., L.M. Hablitz, A.L.R. Xavier, W. Feng, W. Zou, T. Pu, H. Monai, G. Murlidharan, R.M.C. Rivera, M.J. Simon, et al. 2018. Aquaporin-4-dependent glymphatic solute transport in the rodent brain. *Elife.* 7:1–31: e40070. https://doi.org/10.7554/eLife.40070

Patel, T.K., L. Habimana-Griffin, X. Gao, B. Xu, S. Achilefu, K. Alitalo, C.A. McKee, P.W. Sheehan, E.S. Musiek, C. Xiong, et al. 2019. Dural lymphatics regulate clearance of extracellular tau from the CNS. *Mol. Neurodegener.* 14:11–19. https://doi.org/10.1186/s13024-019-0312-x

Pooler, A.M., E.C. Phillips, D.H.W. Lau, W. Noble, and D.P. Hanger. 2013. Physiological release of endogenous tau is stimulated by neuronal activity. *EMBO Rep.* 14:389–394. https://doi.org/10.1038/embor.2013.15

Rauch, J.N., G. Luna, E. Guzman, M. Audouard, C. Challis, Y.E. Sibih, C. Leshuk, I. Hernandez, S. Wegmann, B.T. Hyman, et al. 2020. LRP1 is a master regulator of tau uptake and spread. *Nature.* 580:381–385. https://doi.org/10.1038/s41586-020-2156-5

Ringstad, G., L.M. Valnes, A.M. Dale, A.H. Pripp, S.S Vatnehol, K.E. Emblem, K.A. Mardal, and P.K. Eide. 2018. Brain-wide glymphatic enhancement and clearance in humans assessed with MRI. *JCI Insight.* 3:e121537. https://doi.org/10.1172/jci.insight.121537

Ringstad, G., S.A.S. Vatnehol, and P.K. Eide. 2017. Glymphatic MRI in idiopathic normal pressure hydrocephalus. *Brain.* 140:2691–2705. https://doi.org/10.1093/brain/awx191

Sato, C., N.R. Barthélemy, K.G. Mawuenyega, B.W. Patterson, B.A. Gordon, J. Jockel-Balsarotti, M. Sullivan, M.J. Crisp, T. Kasten, K.M. Kirmess, et al. 2018. Tau kinetics in neurons and the human central nervous system. *Neuron.* 97:1284–1298.e7. https://doi.org/10.1016/j.neuron.2018.02.015

Tanaka, Y., K. Yamada, K. Satake, I. Nishida, M. Heuberger, T. Kuwahara, and T. Iwatsubo. 2019. Seeding activity-based detection uncovers the different release mechanisms of seed-competent tau versus inert tau via lysosomal exocytosis. *Front. Neurosci.* 13:1258–1267. https://doi.org/10.3389/fnins.2019.01258

Wang, J., W.S. Jin, X. Le Bu, F. Zeng, Z.L. Huang, W.W. Li, L.L. Shen, Z.Q. Zhuang, Y. Fang, B.L. Sun, et al. 2018. Physiological clearance of tau in the periphery and its therapeutic potential for tauopathies. *Acta Neuropathol.* 136:525–536. https://doi.org/10.1007/s00401-018-1891-2

Wu, J.W., S.A. Hussaini, I.M. Bastille, G.A. Rodriguez, A. Mrejeru, K. Rilett, D.W. Sanders, C. Cook, H. Fu, R.A.C.M. Boonen, et al. 2016. Neuronal activity enhances tau propagation and tau pathology in vivo. *Nat. Neurosci.* 19:1085–1092. https://doi.org/10.1038/nn.4328

Xie, L., H. Kang, Q. Xu, M.J. Chen, Y. Liao, M. Thiyagarajan, J. O'Donnell, D.J. Christensen, C. Nicholson, J.J. Iliff, et al. 2013. Sleep drives metabolite clearance from the adult brain. *Science.* 342:373–377. https://doi.org/10.1126/science.1241224

Xu, Z., N. Xiao, Y. Chen, H. Huang, C. Marshall, J. Gao, Z. Cai, T. Wu, G. Hu, and M. Xiao. 2015. Deletion of aquaporin-4 in APP/PS1 mice exacerbates brain Aβ accumulation and memory deficits. *Mol. Neurodegener.* 10:58. https://doi.org/10.1186/s13024-015-0056-1

Yamada, K., J.R. Cirrito, F.R. Stewart, H. Jiang, M.B. Finn, B.B. Holmes, L.I. Binder, E.-M. Mandelkow, M.I. Diamond, V.M.-Y. Lee, and D.M. Holtzman. 2011. In vivo microdialysis reveals age-dependent decrease of brain interstitial fluid tau levels in P301S human tau transgenic mice. *J. Neurosci.* 31:13110–13117. https://doi.org/10.1523/JNEUROSCI.2569-11.2011

Yamada, K., J.K. Holth, F. Liao, F.R. Stewart, T.E. Mahan, H. Jiang, J.R. Cirrito, T.K. Patel, K. Hochgräfe, E.-M. Mandelkow, and D.M. Holtzman. 2014. Neuronal activity regulates extracellular tau in vivo. *J. Exp. Med.* 211:387–393. https://doi.org/10.1084/jem.20131685

Yamada, K., T.K. Patel, K. Hochgräfe, T.E. Mahan, H. Jiang, F.R. Stewart, E.-M. Mandelkow, and D.M. Holtzman. 2015. Analysis of in vivo turnover of tau in a mouse model of tauopathy. *Mol. Neurodegener.* 10:55. https://doi.org/10.1186/s13024-015-0052-5

Yanamandra, K., N. Kfoury, H. Jiang, T.E. Mahan, S. Ma, S.E. Maloney, D.F. Wozniak, M.I. Diamond, and D.M. Holtzman. 2013. Anti-tau antibodies that block tau aggregate seeding in vitro markedly decrease pathology and improve cognition in vivo. *Neuron.* 80:402–414. https://doi.org/10.1016/j.neuron.2013.07.046

Yanamandra, K., T.K. Patel, H. Jiang, S. Schindler, J.D. Ulrich, A.L. Boxer, B.L. Miller, D.R. Kerwin, G. Gallardo, F. Stewart, et al. 2017. Anti-tau antibody administration increases plasma tau in transgenic mice and patients with tauopathy. *Sci. Transl. Med.* 9:eaal2029. https://doi.org/10.1126/scitranslmed.aal2029

Yoshiyama, Y., M. Higuchi, B. Zhang, S.M. Huang, N. Iwata, T.C. Saido, J. Maeda, T. Suhara, J.Q. Trojanowski, and V.M.Y. Lee. 2007. Synapse loss and microglial activation precede tangles in a P301S tauopathy mouse model. *Neuron.* 53:337–351. https://doi.org/10.1016/j.neuron.2007.01.010

Zeppenfeld, D.M., M. Simon, J.D. Haswell, D. D'Abreo, C. Murchison, J.F. Quinn, M.R. Grafe, R.L. Woltjer, J. Kaye, and J.J. Iliff. 2017. Association of perivascular localization of aquaporin-4 with cognition and Alzheimer disease in aging brains. *JAMA Neurol.* 74:91. https://doi.org/10.1001/jamaneurol.2016.4370

Supplemental material

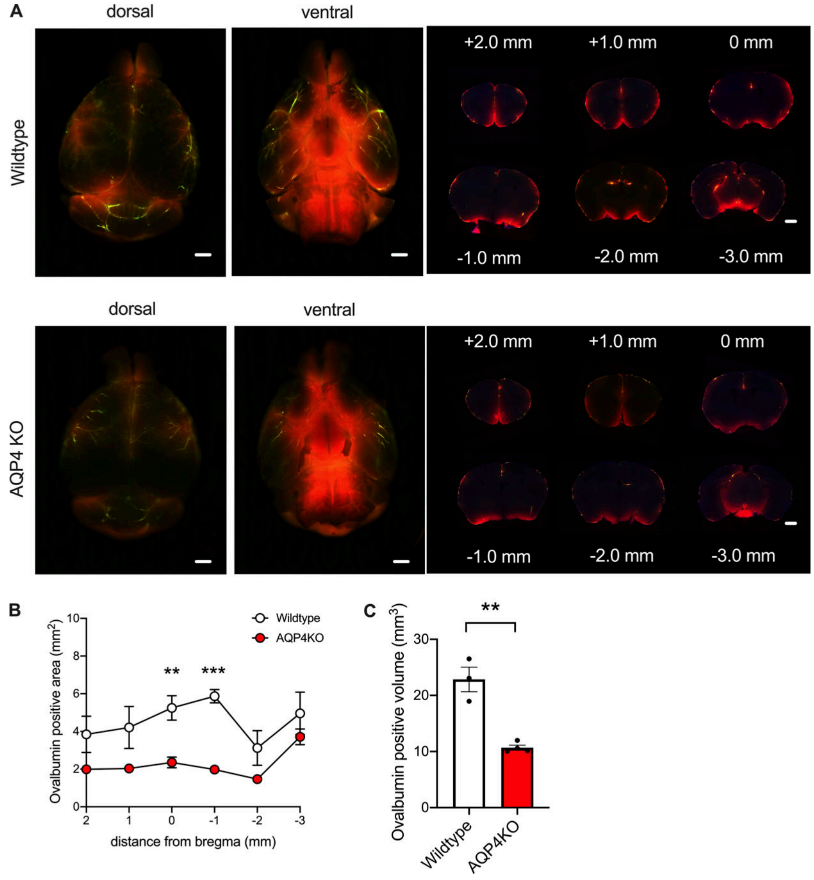

Figure S1. **Ovalbumin influx from CSF to brain in WT mice and AQP4 KO mice. (A)** Representative dorsal and ventral images of ovalbumin (green) and dextran (red) accumulation in WT mice or AQP4 KO mice. Scale bars, 1 mm. **(B)** Ovalbumin-positive area (mm^2) was plotted from different distances to the bregma of WT mice and AQP4 KO mice. WT mice (*n* = 3), AQP4 KO mice (*n* = 4). Two-way ANOVA with Bonferroni post-hoc analysis; **, $P < 0.01$; ***, $P < 0.001$. **(C)** Ovalbumin-positive brain volume (mm^3) at 1 h from injection in WT mice and AQP4 KO mice. Unpaired two-tailed *t* test; **, $P < 0.01$. WT mice (*n* = 3), AQP4 KO mice (*n* = 4).

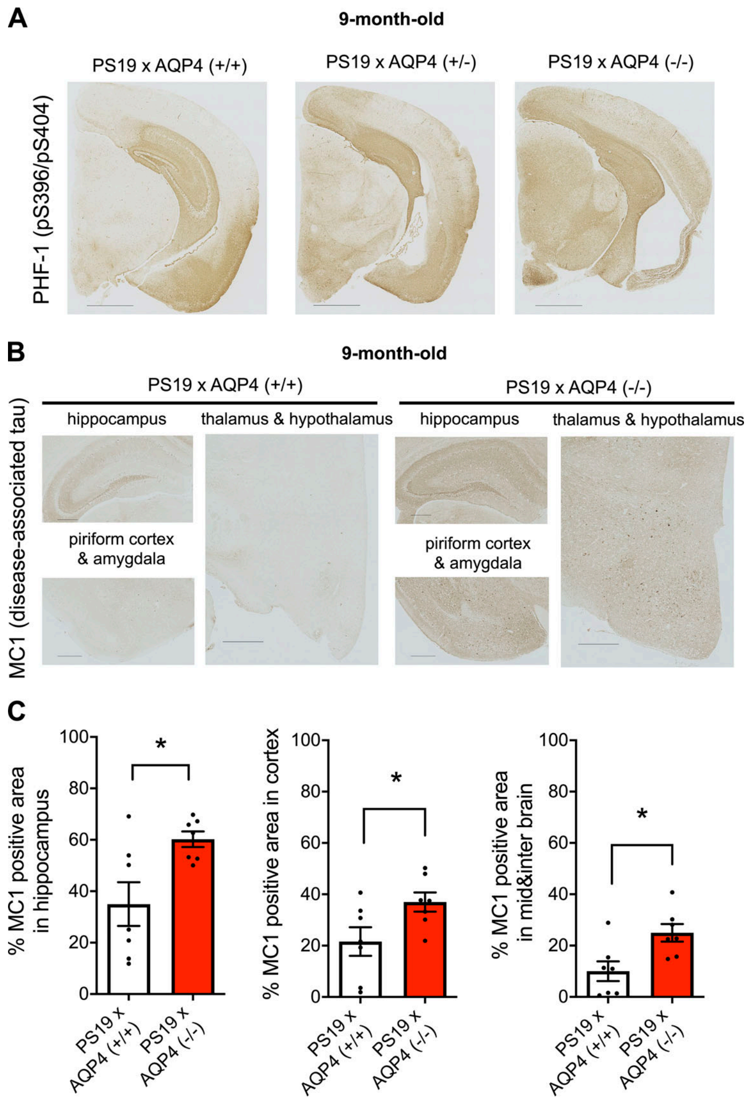

Figure S2. **AQP4 deficiency markedly increases tau pathology stained with PHF-1 and MC1 in PS19 mice. (A)** Representative images of 9-month-old PS19 × AQP4 (+/+), PS19 × AQP4 (+/−), and PS19 × AQP4 (−/−) mice stained with PHF-1. Scale bars, 1 mm. **(B)** Representative images of 9-month-old PS19 × AQP4 (+/+) and PS19 × AQP4 (−/−) mice stained with MC1. Scale bars, 300 µm. **(C)** Quantification of the percentage of area covered by MC1 staining in 9-month-old mice. Unpaired two-tailed *t* test; *, P < 0.05. *n* = 7/group.

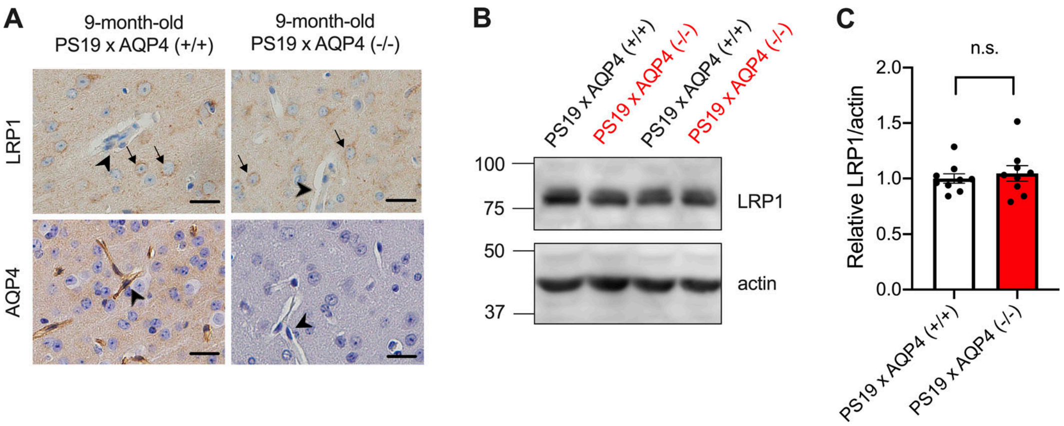

Figure S3. **LRP1 expression was comparable in PS19 mice regardless of AQP4 genotypes. (A)** Representative images of 9-month-old PS19 × AQP4 (+/+) and PS19 × AQP4 (−/−) mice stained with LRP1 or AQP4. Arrows indicate neuronal staining and arrowheads indicate vasculatures. Scale bars, 20 µm. **(B and C)** Representative immunoblots (in kD) probing for LRP1 and actin in RIPA fractions of 9-month-old PS19 × AQP4 (+/+) (*n* = 9) and PS19 × AQP4 (−/−) (*n* = 9) and its quantification. Unpaired two-tailed *t* test; n.s., not significant. Source data are available for this figure: SourceData FS3.